Chemical Engineering Journal 442 (2022) 135876

Contents lists available at ScienceDirect

Chemical Engineering Journal

journal homepage: www.elsevier.com/locate/cej

Combustion characteristics of aluminum particle jet flames in a hot co-flow

Jiarui Zhang [a], Zhixun Xia [a], Oliver T. Stein [b], Likun Ma [a,*], Fei Li [c], Yunchao Feng [a], Zihao Zhang [a], Andreas Kronenburg [b]

[a] College of Aerospace Science and Engineering, National University of Defense Technology, Changsha, Hunan 410073, PR China
[b] Institut für Technische Verbrennung, Universität Stuttgart, Pfaffenwaldring 31, 70569 Stuttgart, Germany
[c] State Key Laboratory of High Temperature Gas Dynamics, Institute of Mechanics, Chinese Academy of Sciences, Beijing, 100190, PR China

ARTICLE INFO

Keywords:
Energy carrier
Aluminum(Al) particle combustion
Particle cloud
Jet flame
Tunable diode laser absorption spectroscopy

ABSTRACT

Aluminum (Al) powder has been proposed as a promising dense energy carrier to store and transport abundant renewable power for a future carbon-neutral society. In this work, a detailed model for simulating Al particle cloud combustion with multiple oxidizers in the context of large eddy simulation is developed. The Al particles are tracked in the lagrangian framework with various sub-models including phase change, heterogeneous surface reaction, evaporation and radiation. The model is then employed to simulate turbulent jet flames with Al particles (d_{32} = 25 μm) in a hot co-flow. Tunable diode laser absorption spectroscopy (TDLAS) is used to measure the temperature and H_2O distribution. The present model is first validated by comparing the predicted condensed Al_2O_3 distribution with the measured Mie scattering signals. The results indicate that the simulation results are in good agreement with the experimental measurements. Further comparisons of the temperature and H_2O profile are then conducted. The numerical simulation predicts weaker mass and heat transport in the upstream and middle of the flame along the centerline of the burner, compared with the reconstructed TDLAS results, but the downstream scalar profiles of the jet flame agree well with the measurements. Discrete characteristics are observed in the simulated instantaneous temperature and condensed Al_2O_3 snapshots, which are due to the nature of heterogeneous combustion of metal fuel particles under fuel-lean conditions. Finally, the influence of the oxidizer mole fraction and the initial temperature of the primary jet on the ignition distance is analyzed. The results demonstrate that the ignition distance can be decreased effectively by increasing the oxidizer concentration of the hot co-flow or the initial temperature of the Al particles and carrier gas.

1. Introduction

For the aim of energy saving and emission reduction, the world needs to reduce its dependence on fossil fuels and increase the use of clean and renewable energy. This requires us to resolve the intermittent nature of renewable energy (such as wind and solar) and the geographic mismatch between its supply and demand [1]. Recently, metal fuels are found to be promising energy carriers for storing and transporting abundant power from renewable sources [2,3]. In this application scenario, metal particles can be burned with air or reacted with water to release their chemical energy at a range of power-generation scales [4], while the combustion products are mainly solid oxide, which can be easily captured and then reduced using renewable energy. Among all potential fuels, such as aluminum [5], iron [6] and boron [7], aluminum (Al) is particularly popular because of its high specific energy [8], environmentally benign products and most importantly, Al particles can be stored for a long time due to its strong corrosion resistance and transported to any distance like fossil fuels.

The underlying combustion mechanisms of Al particles are of great significance for the study of its basic mechanisms [9], and the design of Al powder burners. Starting from the 1950s, significant progress has been achieved in studies of ignition and combustion of single isolated Al particles, Arrhenius-type models [10] for ignition and D^n models [11–13] for combustion have been established, respectively. In contrast, research on the combustion of Al particle clouds gradually emerged in the late 1990s [14]. Much attention has been paid to the study of flame speed of Al suspensions on various experimental configurations, including Bunsen flames [15], spherically-propagating flames [16], tube flames [17], and counterflow flames [18]. An increasing number of numerical simulations [19,20] are carried out on the heterogeneous combustion of Al particle clouds. Most of the existing simulations used a simple burning-time-based method to calculate the burning rate of Al in particle clouds, an approach which requires generalization.

In practical applications, almost all combustors employ turbulent flows in order to increase the flame burning rates [21]. However,

* Corresponding author.
E-mail addresses: zhangjiarui@nudt.edu.cn (J. Zhang), malikun@nudt.edu.cn (L. Ma).

https://doi.org/10.1016/j.cej.2022.135876
Received 8 January 2022; Received in revised form 26 February 2022; Accepted 15 March 2022
Available online 26 March 2022

Nomenclature

Variables

$A_{p,\mathrm{eff}}$	Particle area free of oxide film, m^2
A_r	Pre-exponential factor in the heterogeneous surface reaction model, m/s or s/m
A_s	Particle surface area, m^2
B	Transfer number
C_d	Drag coefficient
C_p	Specific heat of particle, J/(kg K)
D	Diffusion coefficient, m^2/s
d_p	Particle diameter, m
E_a	Activation energy of the heterogeneous surface reaction, J/mol
f	Ratio of deposition rate to mass flow rate around the particle
$f_{Al_2O_3}$	Volumetric fraction of Al_2O_3 smoke
$\boldsymbol{g}$	Gravitational acceleration, m/s^2
G	Incident radiation, W/m^2
h	Total enthalpy, J/kg
$h_{p,HSR}$	Heterogeneous surface reaction enthalpy, J/kg
$h_{p,melt}$	Latent heat of fusion of aluminum, J/kg
k_g	Thermal conductivity of gas phase, W/(m K)
Kn	Knudsen number
k_{sgs}	Subgrid scale kinetic energy, m^2/s^2
L	Path length, m
L_v	latent heat of evaporation, J/kg
m_p	Particle mass, kg
Ma	Mach number
Nu	Nusselt number
Pr	Prandlt number
p	Static pressure, Pa
P_a	Ambient pressure, Pa
$P_{F,sat}$	Saturation pressure of the fuel vapor, Pa
$Q_{p,HSR}$	Heat source due to heterogeneous surface reaction, W
$Q_{p,inter}$	Heat source due to interphase heat transfer, W
$Q_{p,melt}$	Heat source due to solid melting, W
$Q_{p,rad}$	Heat source due to radiation, W
R	Universal gas constant, J/(mol K)
Re_p	Particle's Reynolds number
$\dot{S}_{g,rad}$	Source term in energy equation due to radiation, $J/(m^3\ s)$
$\dot{S}_{h,p}$	Source term due to the energy exchange with dispersed phase, $J/(m^3\ s)$
$\dot{S}_m$	Source term in mass equation of gas phase, $kg/(m^3\ s)$
$\dot{S}_{u_i}$	Source term in momentum equation, $kg/(m^2\ s^2)$
$\dot{S}_{Y_k,reac}$	Source term in species equation, $kg/(m^3\ s)$
$\dot{S}_{Y_k,p}$	Source term due to the mass exchange with diapered phase, $kg/(m^3\ s)$
Sc	Schmidt number
T	Temperature, K
u_i	Velocity in the i th direction, m/s
W	Molecular weight, kg/mol
$\boldsymbol{W}_t$	Wiener term, s^{-1}
X	Mole fraction
X_{eff}	Effective oxidizer mole fraction
Y	Mass fraction

Greek symbols

α	Thermal diffusivity, m^2/s
μ	Dynamic viscosity, kg/(ms)
ν_{st}	Mass stoichiometric ratio
ε_p	Emissivity
κ	Absorption coefficient if the gray gas, 1/m
ρ	Density, kg/m^3
σ	Stefan–Boltzman constant, $W/m^2/K^4$
Θ_r	Eulerian phase temperature, K
ω_k	Source term in species equation due to homogeneous reaction, $kg/(m^3\ s)$
τ_{ij}	Viscous stress tensor, Pa
ζ	Fraction of the aluminum sphere covered by the oxide cap

Subscripts

Al_2O_3	Alumina
Al	Aluminum
$Al_2O_3(l)$	Condensed alumina
F	Fuel
g	Gas property
p	Particle property
s	Particle surface

Abbreviations

HSR	Heterogeneous surface reaction
LES	Large eddy simulation
TDLAS	Tunable diode laser absorption spectroscopy

the experimental literature on metal fuels in particle clouds under turbulent conditions is rather scarce [22,23]. The difficulties of this type of experiment are due to the fact that Al particles have a high ignition temperature [24], and thus a relatively long preheating stage. As a result, it is difficult for Al/air suspensions to burn self-sustainably under high-Reynolds-number turbulent conditions. Therefore, a hot co-flow is needed to achieve a stable Al particle jet flame [23]. On the other hand, with the development of computational fluid dynamics, Large Eddy Simulation (LES) has become an attractive tool to study the underlying physical and chemical processes inside different combustors, and such technology has been widely used in the fields of gas fuel combustion [25], spray combustion [26] and pulverized coal combustion [27]. However, LES of the combustion of Al or other metal particle clouds is seldomly reported, and most existing numerical studies [28,29] regarding Al particle combustion under turbulent conditions are for solid rocket engines, which is based on Reynolds-Averaged Navier Stokes (RANS) approach. Such RANS techniques are useful for order-of-magnitude estimates, give an indication of the mean flow and scalar quantities, but cannot capture unsteady physical features such as flame ignition characteristics [30].

Therefore, the objective of the present study is (1) to extend our previous study [31] with a single oxidant to multiple ones, (2) to couple the proposed model to the LES framework and (3) to investigate the flame structure of Al particle jet flames stabilized in a hot co-flow

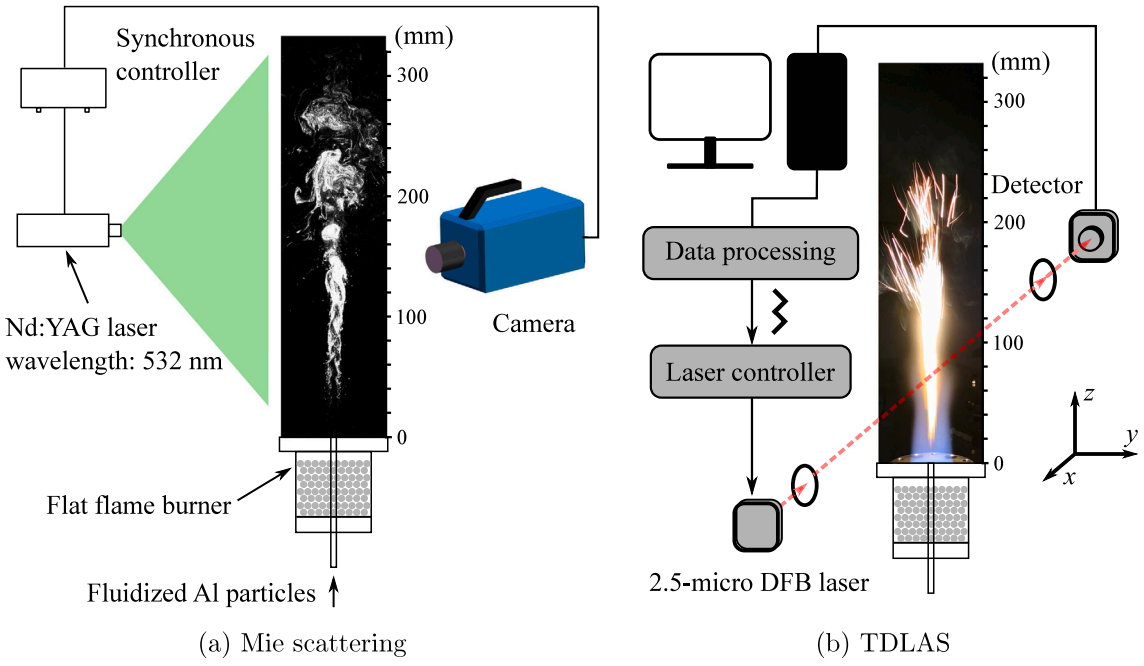

Fig. 1. Schematic diagram of the optical diagnostic system for the aluminum particle jet flame.

supported by a flat flame burner by means of both numerical simulation and experimental measurement. The present model is first validated by comparing the predicted condensed Al_2O_3 distribution and the measured Mie scattering signals. Further validation is then conducted by comparison of the predicted temperature and H_2O profiles with the experimental results. Moreover, the flame structure and the effects of oxidizer concentration on the ignition distance are investigated and discussed in detail.

Table 1
Spectroscopic line parameters of H_2O transitions.

Transitions	Wavelength (nm)	Frequency (cm^{-1})	Line strength (atm^{-1} cm^{-2})	Low-state energy (cm^{-1})
1	2481.69	4029.52	1.10×10^{-4}	2660.94
2	2481.08	4030.50	2.25×10^{-9}	4902.61
	2480.94	4030.73	2.68×10^{-9}	4889.49

2. Experimental method

Fig. 1(a) illustrates a schematic diagram of the Al particle jet flame with our Mie scattering diagnostic system, and it is basically the same as the one used in our previous study [23]. The Al particles are fluidized by a particle feeder to form a gas-solid flow, which is then fed into the post-flame gas supported by a premixed (methane, air and oxygen) flat-flame burner. The particle feeding rate is pre-calibrated with a deviation of less than 12% for the studies conditions. Then, the dust concentration at the particle inlet is calculated as Al particle mass flow rate divided by fluidizing gas flow rate. A Nd:YAG laser at a wavelength of 532 nm is used to illuminate the particles and condensed phase product via Mie scattering. Detailed information on this experimental setup can be found in Ref. [23].

As a non-invasive measurement technology, Tunable Diode Laser Absorption Spectroscopy (TDLAS) is a promising approach to quantify the time-resolved temperature and partial pressure of target gas species. Fig. 1(b) shows a schematic diagram of the TDLAS diagnostic system for the Al jet flames, and the same optical setup has been proven to be able to determine the temperature of the exhaust gas of a hybrid rocket, which comprises a combination of solid fuel and liquid oxidizer, with an uncertainty of 2.24% [32,33]. Details of the absorption spectroscopy theory and the TDLAS system can be found in Refs. [32,33], and only a brief description is presented here.

Variations in temperature and H_2O partial pressure of the Al jet flames at different heights were determined based on H_2O absorption near 2.5 μm. A single distributed feedback (DFB) laser (Nanoplus GmbH) centered near 2.5 μm was deployed with a stable output power of 10 mW to probe the H_2O transitions listed in Table 1, which provides suitable spectral windows for TDLAS sensing with minimal CO_2 interference and good signal-to-noise ratio at harsh conditions. The current of the DFB laser was modulated by a ramp signal of 2 kHz provided by a function generator. The output laser beam was collimated to a beam waist diameter of approximately 0.5 mm. The transmitted light was then split into two beams. Part of the laser beam passed through a narrow-band filter (with a center wavelength of 2.5 μm and bandwidth of 50 nm) and an iris to mitigate the influence of background radiation. A focusing lens was used to collimate the collected light to further enhance the transmitted signal. The other part of the laser beam was directed into a Fabry–Perot interferometer to calibrate the absolute wavelength. Then, these two laser beams were simultaneously monitored by photodetectors, and the detector outputs were recorded by a data processing module at a sampling rate of 2 MHz. All the diagnostic devices were fixed on a frame, and a stepping motor was used to drive the measurement system to reciprocate along the y axis once at each height with a velocity of 1 cm/s after the flame was stabilized. By comparing the two sets of data obtained by reciprocating scanning in one experiment, it is proved that the flame has good time stability. Finally, the radial distribution of the gas temperature profile was obtained from Abel deconvolution.

The size distribution of Al particles used in the experiments with a Sauter mean diameter (d_{32}) of 25 μm was measured by a laser diffraction particle size analyzer, in which 17 particle size bins are obtained, as shown in Fig. 2. The exact same 17 particle size bins are used for the numerical simulations where all particles are tracked individually without particle clustering.

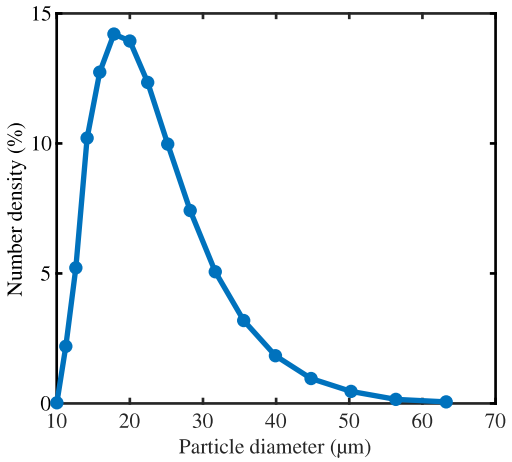

Fig. 2. Size distribution of Al particle used in the experiments.

3. Numerical modeling

3.1. Governing equations of the gas phase

Based on spatial and Favre-filtering operations, the filtered governing equations of the gas phase can be written as [34],

$$\frac{\partial \bar{\rho}}{\partial t} + \frac{\partial \bar{\rho}\widetilde{u_i}}{\partial x_i} = \bar{S}_m \tag{1}$$

$$\frac{\partial \left(\bar{\rho}\tilde{u}_i\right)}{\partial t} + \frac{\partial \bar{\rho}\tilde{u}_i\tilde{u}_j}{\partial x_j} = \frac{\partial}{\partial x_j}\left[\bar{\tau}_{ij} - \bar{\rho}\left(\widetilde{u_i u_j} - \tilde{u}_i\tilde{u}_j\right)\right] - \frac{\partial \bar{p}}{\partial x_i} + \bar{\rho}g_i + \bar{S}_{u_i} \tag{2}$$

$$\frac{\partial(\bar{\rho}\tilde{h})}{\partial t} + \frac{\partial}{\partial x_i}\left(\bar{\rho}\tilde{u}_i\tilde{h}\right) = \frac{\partial}{\partial x_i}\left[\bar{\rho}\tilde{\alpha}\frac{\partial \tilde{h}}{\partial x_i} - \bar{\rho}\left(\widetilde{u_i h} - \tilde{u}_i\tilde{h}\right)\right] + \bar{S}_{h,p} + \bar{S}_{g,rad} \tag{3}$$

$$\frac{\partial \bar{\rho}\widetilde{Y}_k}{\partial t} + \frac{\partial}{\partial x_i}\left(\bar{\rho}\tilde{u}_i\widetilde{Y}_k\right) = \frac{\partial}{\partial x_i}\left[\bar{\rho}\tilde{D}\frac{\partial \widetilde{Y}_k}{\partial x_i} - \bar{\rho}\left(\widetilde{u_i Y_k} - \tilde{u}_i\widetilde{Y}_k\right)\right] + \bar{\omega}_k + \bar{S}_{Y_k,p} \tag{4}$$

where $\bar{S}_m$, $\bar{S}_{u_i}$, $\bar{S}_{h,p}$ and $\bar{S}_{Y_k,p}$ are the source terms from the dispersed phase, $\bar{S}_{g,rad}$ and $\bar{\omega}_k$ are the source terms due to radiation and homogeneous reaction, respectively. The sub-grid scale stress tensor in the filtered momentum equation (Eq. (2)) is modeled by the Smagorinsky model [35]. The unclosed terms in Eqs. (2)–(4) are treated as enhanced diffusion terms by employing an eddy-viscosity modeling concept with sub-grid Schmidt and Prandtl numbers both equal to 0.4 [36].

3.2. Governing equations of the dispersed phase

Al particles are treated in a Lagrangian manner following the laws of motion for dispersed flow and the fundamental processes of heat and mass exchange with their surroundings. The whole conversion process of the Al particle is modeled in two stages. In the first stage (see Fig. 3), namely preheating and heterogeneous reaction stage, the particle is heated by the hot environment via interphase and radiative heat transfer followed by melting. Heterogeneous Surface Reaction (HSR) occurs after liquid Al has been formed and provides further heat until the oxide layer is completely melted and forms an oxide cap. In this stage, the product of HSR, i.e., Al_2O_3, is assumed to be directly deposited on the particle and remains part of the Lagrangian particle. In the second stage (see Fig. 4), namely the quasi-steady combustion stage, after the oxide film is removed, the molten Al is exposed to the oxidizing gas, and a detached diffusion flame is established around the particle. In this stage, evaporated Al vapor ($\dot{m}_{\mathrm{Al}}$) reacts with CO_2, H_2O and O_2 via homogeneous reactions and part of the final product ($\dot{m}_{\mathrm{dep}}$), i.e., Al_2O_3, is deposited on the particle surface, which increases the size of the oxide cap. The other part of Al_2O_3 is released to the bulk gas and exists as fine smoke [20]. The modeling strategy of closing $\dot{m}_{\mathrm{Al}}$ and $\dot{m}_{\mathrm{dep}}$ will be presented in Section 3.2.2.

3.2.1. Preheating and heterogeneous reaction stage

Considering drag force, gravity and the effect of sub-grid fluctuations, the particle momentum equation under turbulent condition reads

$$d\boldsymbol{u}_p = \frac{\tilde{\boldsymbol{u}}_g - \boldsymbol{u}_p}{\tau_p}dt + \boldsymbol{g}dt + \sqrt{C_0\frac{k_{sgs}}{\tau_t}}d\boldsymbol{W}_t \tag{5}$$

$$\tau_p = \frac{3}{4}\frac{\mu}{\rho_p d_p^2}C_D \tag{6}$$

where C_D is the drag coefficient given in Ref. [37], $\boldsymbol{g}$ is the gravitational acceleration, C_0 on the third term in the RHS is a model constant assigned a value of unity [38], k_{sgs} is the subgrid scale kinetic energy of the gas phase, τ_t is the sub-grid time scale for the rate of interaction between particles and small-scale turbulence [39], $d\boldsymbol{W}_t$ is the increment of the Wiener process.

The evolution of the particle temperature, T_p, in the first stage is written as

$$m_p c_{p,p}\frac{dT_p}{\mathrm{d}t} = \dot{Q}_{p,inter} + \dot{Q}_{p,melt} + \dot{Q}_{p,HSR} + \dot{Q}_{p,rad} \tag{7}$$

where $c_{p,p}$ is the specific heat of the particle. $\dot{Q}_{p,inter}$, $\dot{Q}_{p,melt}$, $\dot{Q}_{p,HSR}$ and $\dot{Q}_{p,rad}$ are source terms of particle temperature due to interphase heat transfer, melting, HSR and radiation respectively.

$\dot{Q}_{p,inter}$ in Eq. (7) is the interphase heat transfer rate calculated by

$$\dot{Q}_{p,inter} = \pi d_p k_g\left(T_g - T_p\right)Nu_p \tag{8}$$

where Nu_p is the Nusselt number that can be calculated from the Ranz-Marshall model [40]

$$Nu_{p,Ranz} = 2 + 0.6Re_p^{\frac{1}{2}}Pr_p^{\frac{1}{3}}. \tag{9}$$

and a modification of Nusselt number [41] is introduced to cover the transit heat transfer regime, which reads

$$Nu_{p,Kava} = \frac{Nu_{p,Ranz}}{1 + 3.42Nu_{p,Ranz}\frac{Ma}{Re_p Pr_p}} \tag{10}$$

where Ma is the Mach number.

When the particle temperature reaches the melting point of Al or Al_2O_3 and the corresponding solid mass fraction of the particle is greater than zero, the left hand side of Eq. (7) is zero and the melting rate can be calculated as

$$\dot{m}_{p,melt} = -\frac{\dot{Q}_{p,melt}}{h_{p,melt}} = \frac{\dot{Q}_{p,inter} + \dot{Q}_{p,HSR} + \dot{Q}_{p,evap} + \dot{Q}_{p,rad}}{h_{p,melt}} \tag{11}$$

where $h_{p,melt}$ is the latent heat of fusion [42].

Three global HSRs are employed in the present study

$$\mathrm{Al(l)} + 0.75\mathrm{O_2(g)} \rightarrow 0.5\mathrm{Al_2O_3(s\ or\ l)} \tag{12}$$

$$\mathrm{Al(l)} + 1.5\mathrm{H_2O(g)} \rightarrow 0.5\mathrm{Al_2O_3(s\ or\ l)} + 1.5\mathrm{H_2(g)} \tag{13}$$

$$\mathrm{Al(l)} + 0.75\mathrm{CO_2(g)} \rightarrow 0.5\mathrm{Al_2O_3(s\ or\ l)} + 0.75\mathrm{C(s)} \tag{14}$$

with the consumption rates of Al by HSRs with different oxidizers

$$\dot{m}_{p,HSR}^{Al,ox} = A_{p,\mathrm{eff}}\rho_s Y_{ox,s}A_r\exp\left(-\frac{E_a}{RT_p}\right),\ ox = \mathrm{O_2, H_2O} \tag{15}$$

and

$$\dot{m}_{p,HSR}^{Al,ox} = A_{p,\mathrm{eff}}P_{ox,s}A_r\exp\left(-\frac{E_a}{RT_p}\right),\ ox = \mathrm{CO_2} \tag{16}$$

where ρ_s and $P_{ox,s}$ are the gas density and the partial pressure of the oxidizer on the particle surface, respectively. $A_{p,\mathrm{eff}}$ is the surface area of the Al core, the diameter of which is calculated as [20]

$$d_{p,Al} = \sqrt[3]{\frac{6m_{p,\mathrm{Al}}}{\pi\rho_{\mathrm{Al}}}} \tag{17}$$

and other parameters in Eqs. (15) and (16) are listed in Table 2

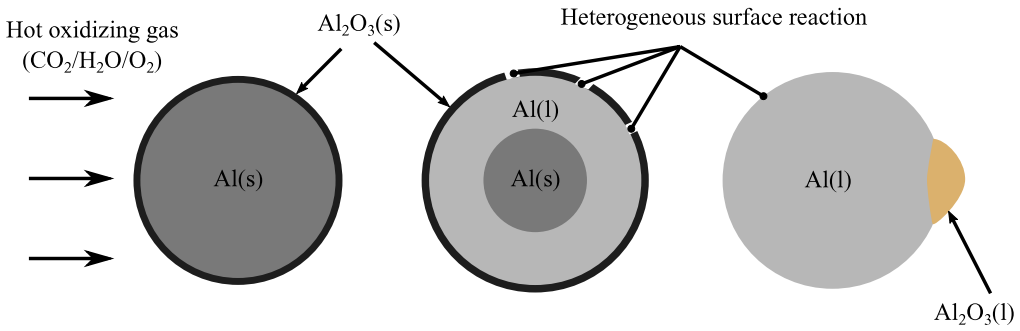

Fig. 3. Schematic diagram of preheating and heterogeneous reaction stage.

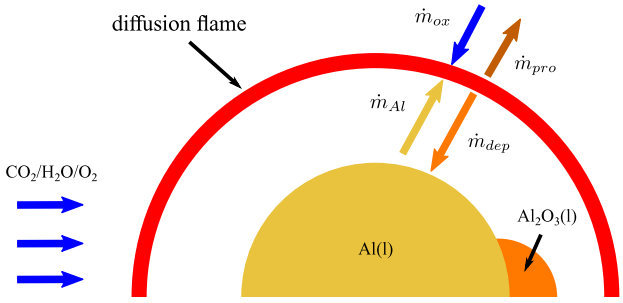

Fig. 4. Schematic diagram of quasi-steady combustion stage.

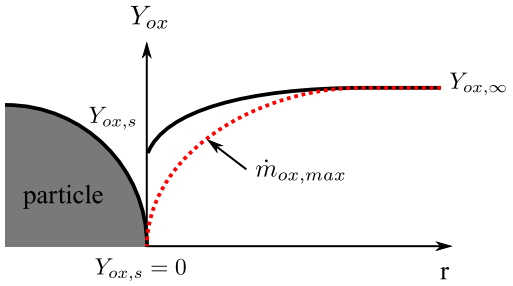

Fig. 5. Schematic diagram of the diffusion of oxidizers from the bulk gas to the particle surface. The red dashed line presents the case of maximum diffusion rate at a given oxidizer concentration in the bulk gas.

Table 2
Parameters used in the heterogeneous surface reaction model of aluminum.

Oxidizer	A_r	E_a
O_2	1.8E+04 (m/s)	8.4E+7 (J/kmol)
H_2O	1.4E+04 (m/s)	8.4E+7 (J/kmol)
CO_2	3.9E+02 (s/m)	1.5E+8 (J/kmol)

The HSR model in Eqs. (15) and (16) consider a completely kinetically-controlled reaction rate, which may lead to unrealistically large mass consumption of Al. Therefore, a simple oxygen diffusion model is employed in the present study to provide an estimation of the maximum reaction rate of HSR [43]. As shown in Fig. 5, the concentration of the oxidizers in the far field and at the particle surface are $Y_{ox,\infty}$ and $Y_{ox,s}$ respectively. The diffusion rate of oxidizers from the bulk gas to the particle surface can be calculated as [43]

$$\dot{m}_{ox} = A_p \frac{Sh\rho_g D_{ox}}{d_p}\left(Y_{ox,\infty} - Y_{ox,s}\right) \quad , \quad ox = O_2, CO_2, H_2O \tag{18}$$

and a maximum diffusion rate of oxygen can be obtained when $Y_{O_2,s} = 0$, which is denoted as $\dot{m}_{ox,max}$. Therefore, the modified HSR reaction rate can be expressed as follows,

$$\dot{m}^{Al,ox}_{p,surf} = \min\left(\dot{m}'^{Al,ox}_{p,HSR}, \frac{\dot{m}_{ox,max}}{\nu_{st,ox}}\right), \quad ox = O_2, CO_2, H_2O \tag{19}$$

where $\nu_{st,ox}$ is the mass stoichiometric ratio for different oxidizers. Finally, the heat release rate due to HSRs can be calculated as

$$\dot{Q}_{p,HSR} = \sum_{ox}\left(\dot{m}^{Al,ox}_{p,HSR} h^{ox}_{p,HSR}\right), \quad ox = O_2, CO_2, H_2O \tag{20}$$

where $h^{ox}_{p,HSR}$ is the reaction heat of HSR, which is calculated based on the enthalpy difference of the products and reactants and dynamically updated as a function of temperature.

Under the assumption of gray gas with negligible scattering and gray particles with scattering effect, radiation is considered in both stages of the aluminum conversion process by solving the radiative transfer equation (RTE) [44] in the present study. Since the condensed phase Al_2O_3 is modeled as a continuous Eulerian species, following the modeling strategy of the radiative heat transfer with soot [45] the continuous mixture absorption coefficient, κ_m, is calculated as

$$\kappa_m = \kappa_g + \kappa_{smoke} \tag{21}$$

where κ_g is the gas absorption of the post-flame gas resulting from the flat flame burner, which is calculated using the weighted-sum-of-gray-gases model with the coefficients suggested by Kangwanpongpan et al. [46]. The absorption coefficient of the oxide smoke is assumed to be calculated as

$$\kappa_{smoke} = f_{Al_2O_3}\kappa_{Al_2O_3} \tag{22}$$

where $f_{Al_2O_3}$ is the volumetric fraction of Al_2O_3 smoke, which is approximated by its mole fraction in the gas. The absorption coefficient of Al_2O_3 is obtained from

$$\kappa_{Al_2O_3} = -\frac{\ln\left(1-\varepsilon_{Al_2O_3}\right)}{L} \tag{23}$$

where L is the path length [31], and $\varepsilon_{Al_2O_3}$ the emissivity of alumina, which is calculated by polynomial fitting as a function of temperature using the experimental data from Ref. [47]. The fitting function reads

$$\varepsilon_{Al_2O_3} = \frac{a}{c + \exp\left(-b\left(T_g - 2700\right)\right)} + dT_g \tag{24}$$

with $a = 0.07668$, $b = 0.01504$, $c = 0.1131$ and $d = 4.875\text{E}{-}05$.

The radiative heat exchange terms in Eqs. (7) and (3) are calculated as

$$\dot{Q}_{p,rad} = \varepsilon_p A_p \sigma\left(\Theta_r^4 - T_p^4\right) \tag{25}$$

$$\dot{S}_{g,rad} = 4\kappa_g \sigma\left(\Theta_r^4 - T_g^4\right) \tag{26}$$

where $\varepsilon_p = 0.12$ is the particle emissivity [48] and Θ_r is the Eulerian phase radiation temperature, which is calculated as

$$\Theta_r = \left(\frac{G}{4\sigma}\right)^{1/4} \tag{27}$$

where σ is the Stefan–Boltzman constant. G is the incident radiation, which is calculated by the discrete ordinates method [49] in the present study. It is noted that the same radiation model also applies in the next quasi-steady combustion stage.

3.2.2. Quasi-steady combustion stage

Once the oxide film has coalesced into a cap, a diffusion flame is assumed to be established in a very short time, and reactions shift from the particle surface to the gas phase. Following the modeling strategy in Ref. [50,51], a conserved scalar approach is employed to solve vapor-phase combustion, in which a surface sink term, $\dot{m}_{dep}$, is introduced to account for the deposition of Al_2O_3 on the particle surface. The boundary conditions for the Al particle surface become as follows:

$$\dot{m} = \dot{m}_{\mathrm{Al}} - \dot{m}_{dep} \tag{28}$$

$$\dot{m}_{i,s} = \dot{m} Y_{i,s} - 4\pi r_s^2 \rho D \left(\frac{dY_i}{dr}\right)_{r=r_s} \tag{29}$$

$$4\pi r_s^2 \rho D \left(\frac{d\left(c_p T\right)}{\mathrm{d}r}\right)_{r=r_s} + \dot{Q}_{p,rad} + \dot{Q}_{p,dep} = \dot{m}_{\mathrm{Al}} L_v \tag{30}$$

where L_v is the latent heat of evaporation of Al, and $\dot{Q}_{p,dep}$ is the source term due to Al_2O_3 deposition, which reads

$$\dot{Q}_{p,dep} = \dot{m}_{\mathrm{dep}} \Delta h_{\mathrm{Al_2O_3}} \tag{31}$$

with the enthalpy difference of Al_2O_3 before and after deposition $\Delta h_{\mathrm{Al_2O_3}}$.

Similar to the classical hydrocarbon droplet analysis [52], the total mass flow rate in convective environment can be expressed as:

$$\dot{m} = \pi d_{\mathrm{p,Al}} \rho D Sh \ln(1+B) \tag{32}$$

with transfer number B. In order to determine the transfer number, three conserved scalars can be derived from the spherically symmetrical governing equations of the gas phase around the particle, which reads

$$\beta_{\mathrm{Al-ox}} = Y_{\mathrm{Al}} - \sum_{ox} \frac{Y_{\mathrm{ox}}}{\nu_{st,\mathrm{ox}}},\ \mathrm{ox} = \mathrm{O_2}, \mathrm{CO_2}, \mathrm{H_2O} \tag{33}$$

$$\beta_{\mathrm{Al-Al_2O_3}} = Y_{\mathrm{Al}} - \frac{Y_{\mathrm{Al_2O_3}}}{\nu_{st,\mathrm{Al_2O_3}}} \tag{34}$$

$$\beta_{\mathrm{Al-T}} = c_p T - \sum_{ox} \frac{Y_{\mathrm{ox}} Q_{\mathrm{ox}}}{\nu_{st,ox}},\ \mathrm{ox} = \mathrm{O_2}, \mathrm{CO_2}, \mathrm{H_2O} \tag{35}$$

where Q_{ox} is the combustion heat of Al in different oxidizers. It is noted that the heat release due to the formation of condensed Al_2O_3 is included in Q_{ox}, for example, the $Q_{\mathrm{O_2}}$ is calculated as

$$Q_{\mathrm{O_2}} = h_{\mathrm{Al}} + 0.75 \frac{W_{\mathrm{O_2}}}{W_{\mathrm{Al}}} h_{\mathrm{O_2}} - 0.5 \frac{W_{\mathrm{Al_2O_3}}}{W_{\mathrm{Al}}} h_{\mathrm{Al_2O_3(l)}} \tag{36}$$

where h is the enthalpy which is calculated dynamically based on temperature, W is the molecular weight, Al_2O_3(l) indicates the condensed Al_2O_3(l).

Then the following three transfer numbers can be obtained following the classical hydrocarbon droplet analysis [52],

$$B_{\mathrm{Al-ox}} = \frac{Y_{\mathrm{Al},s} + \sum_{ox}\left(\frac{1}{\nu_{st,\mathrm{ox}}} Y_{\mathrm{ox},\infty}\right)}{f + 1 - Y_{\mathrm{Al},s}},\ \mathrm{ox} = \mathrm{O_2}, \mathrm{CO_2}, \mathrm{H_2O} \tag{37}$$

$$B_{\mathrm{Al-Al_2O_3}} = \frac{-Y_{\mathrm{Al},s} - \frac{1}{\nu_{st,\mathrm{Al_2O_3}}} Y_{\mathrm{Al_2O_3},\infty}}{Y_{\mathrm{Al},s} - \left[\left(1 + \frac{1}{\nu_{st,\mathrm{Al_2O_3}}}\right) f + 1\right]} \tag{38}$$

$$B_{\mathrm{Al-T}} = \frac{c_p\left(T_\infty - T_s\right) - \sum_{ox}\left(\frac{1}{\nu_{st,\mathrm{ox}}} Y_{\mathrm{ox},\infty} Q_{\mathrm{ox}}\right)}{(1+f) L_v - \frac{\dot{Q}_{p,rad} - \dot{Q}_{p,cond}}{\dot{m}}},\ \mathrm{ox} = \mathrm{O_2}, \mathrm{CO_2}, \mathrm{H_2O} \tag{39}$$

where fraction f is defined as $f = \dot{m}_{dep}/\dot{m}$. It should be noted that the above transfer numbers are derived based on the assumptions of $Y_{\mathrm{Al_2O_3},s} = 0$ and $Y_{\mathrm{ox},s} = 0$ [50]. Then, taking into account the hindering effect of the oxide cap on the evaporation of particles, the evaporation rate is calculated as:

$$\dot{m}_{p,evap} = \dot{m}_{\mathrm{Al}} = (1+f)\pi(1-\zeta) d_{\mathrm{p,Al}} \rho D Sh \ln(1+B) \tag{40}$$

and deposition rate:

$$\dot{m}_{p,dep} = \dot{m}_{\mathrm{dep}} = f\pi(1-\zeta) d_{\mathrm{p,Al}} \rho D Sh \ln(1+B) \tag{41}$$

where ζ is the fraction of the aluminum sphere covered by the oxide cap, the model closure of which is given in our previous study [31]. Thus, the mass equation of dispersed phase in the second stage reads,

$$\dot{m}_p = -\dot{m}_{p,evap} + \dot{m}_{p,dep} \tag{42}$$

Assuming that the Al droplet rapidly heats up to a steady temperature, T_p, an expression relating the surface partial pressure of Al vapor to the particle temperature is employed to close the model [53]:

$$T_p = \frac{34860}{12.537 - \ln\left(P_{\mathrm{Al},s}\right)}\ \ (\mathrm{K}) \tag{43}$$

and the partial pressure of Al vapor, $P_{\mathrm{Al},s}$, is obtained using Raoult's Law. Note that an iterative procedure is required to make sure that all three transfer numbers, as shown in Eqs. (37)–(39), are equal.

Although detailed homogeneous kinetics of Al with O_2, H_2O and CO_2 are available in Ref. [54] containing 22 species and 50 reactions, such detailed chemistry is too expensive to solve in the present LES framework. Therefore, the following three global reactions are employed with infinitely fast reaction rate,

$$\mathrm{Al} + 0.75\mathrm{O_2} \rightarrow 0.5\mathrm{Al_2O_3} \tag{44}$$

$$\mathrm{Al} + 1.5\mathrm{H_2O} \rightarrow 0.5\mathrm{Al_2O_3} + 1.5\mathrm{H_2} \tag{45}$$

$$\mathrm{Al} + 1.5\mathrm{CO_2} \rightarrow 0.5\mathrm{Al_2O_3} + 1.5\mathrm{CO} \tag{46}$$

where H_2 and CO are further oxidized to H_2O and CO_2

$$\mathrm{H_2} + 0.5\mathrm{O_2} \rightarrow \mathrm{H_2O} \tag{47}$$

$$\mathrm{CO} + 0.5\mathrm{O_2} \rightarrow \mathrm{CO_2} \tag{48}$$

using the concept of the eddy break up model [55]. This infinitely fast reaction rate modeling for the Al vapor oxidizing reactions (as shown in Eqs. (44)–(46)) is reasonable for metal fuel combustion, because the reaction rate of metal-vapor with oxidizer is very fast [56]. Hence, Al particles can be treated as point sources of heat and mass under the fuel-lean conditions [20]. Moreover, since Al_2O_3 does not prevail as a stable gas phase species, an irreversible reaction is used to describe the transition from gaseous to condensed phase Al_2O_3, denoted as Al_2O_3(l). The condensed Al_2O_3 from homogeneous reaction exists as a very fine smoke and attributed to the Eulerian gas phase, and part of Al_2O_3(l) is deposited on the particle surface, the mass flow rate of which is given by Eq. (41).

4. Numerical details

The computational domain features a three-dimensional cylindrical field with a diameter of 100 mm and a length of 200 mm, as shown in Fig. 6. The particles are fluidized by an air stream and injected from the particle inlet with an inner diameter of 2 mm and an outer diameter of 3 mm. The numerical conditions are shown in Table 3. The post-flame gas is assumed to be the products of complete combustion of methane/air/oxygen mixture with an uniform inlet velocity, which is derived from the gas temperature measured by TDLAS based on the perfect gas assumption. A separate pipe flow using periodic boundary condition was simulated in advance, which provides a fully transient velocity boundary condition for the gas phase of the primary jet in LES. The particle inlet velocity is assumed to have a magnitude identical to that of the average gas velocity at the particle inlet, for example, 15.92 m/s in Case 1 in Table 3. The direction of the particle velocity is

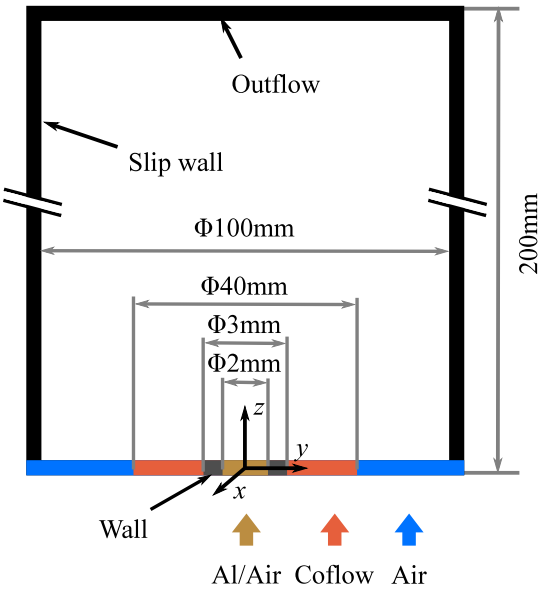

Fig. 6. Computational domain and boundary conditions for the Al particle jet flame in a hot co-flow.

Table 3
Numerical simulation conditions.

No.	Premixed gas			X_{eff}	Carrier gas	T_0	θ	C	Re
	Air L/min	CH_4 L/min	O_2 L/min	%	Air L/min	K	°	g/m^3	–
1	54	7	6	19.82	3	300	22.02	425	2113
2	50	7	10	24.54	3	300	22.02	425	2113
3	46	7	14	29.25	3	300	22.02	425	2113
4	42	7	18	33.97	3	300	22.02	425	2113
5	50	7	10	24.54	6	300	29.06	425	4227
6	50	7	10	24.54	3	500	22.02	425	2113
7	50	7	10	24.54	3	700	22.02	425	2113
8	50	7	10	24.54	6	300	22.02	850	4227

Notes: The effective oxidizer mole fraction is defined by $X_{eff} = X_{O_2} + 0.6X_{H_2O} + 0.22X_{CO_2}$ [11].

randomly distributed within an injection angle measured by the Mie scattering signal, as shown in Fig. 7. The edge of the particle jet is obtained by finding the boundary that envelops 90% of the particles on a certain level, and the inject angle θ is then obtained by fitting the jet edge. It was found that the injection angle is mainly a function of the carrier gas flow rate, therefore, it is assumed that the injection angle remains constant when the carrier gas flow rate is unchanged, as listed in Table 3. The Reynolds number (Re) at outlet of the primary jet can be changed adjusting the carrier gas flow rate, as listed in Table 3. The dust concentration, which is denoted as C in Table 3, at the particle inlet equals to the mass feeding rate of the Al particle divided by the carrier gas flow rate. The initial temperatures of the Al particles and carrier gas are both assumed to be T_0 as listed in Table 3. A small co-flow of air (0.61 m/s) is set to represent possible entrainment. Since the diameter of the domain is much larger than the one of the primary jet, a slip wall condition is imposed on the lateral boundary of the computational domain to enhance simulation stability [57,58]. Additionally, zero-gradient boundary conditions are used at the upper outlet.

Fig. 8 shows the results of the measured gas temperature profile at the flat-flame burner outlet from TDLAS, and the gas temperature for the simulations can be treated as uniformly distributed at 2058 K in the post-gas inlet. Moreover, the post-flame gas temperature is considered to be constant, when the methane gas flow rate and the total gas flow rate are unchanged [23,59].

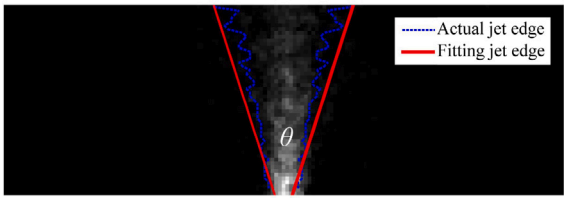

Fig. 7. Particle injection angle obtained by Mie scattering in Case 5 listed in Table 3.

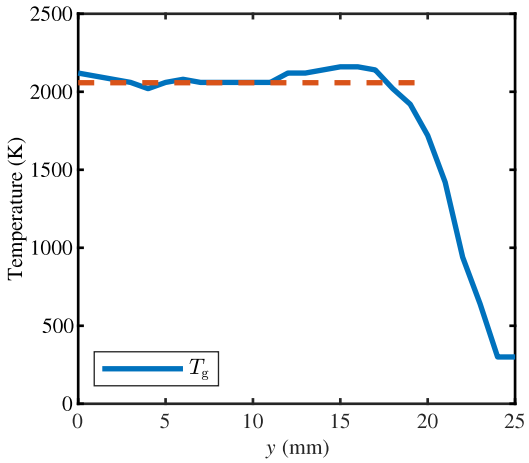

Fig. 8. Temperature distribution of the gas phase at the flat-flame burner outlet (z = 0) in Case 5 listed in Table 3.

The computational domain is initially discretized with 85 × 40 × 200 grid points in the radial, azimuthal and axial directions respectively, then the grid points are doubled three times in three cylindrical regions with a decreasing diameter along the axial direction, resulting in a total mesh size of approximately 2.5 cells. In present study, a first simulation on a coarse mesh with 72 000 cells is run up for 0.5 s of physical time. The initial results were mapped from the coarse mesh onto the fine mesh to obtain a reasonable initial condition. The fine simulations are then run for 0.2 s, until turbulence is fully developed. Another 0.1 s of runtime are simulated to collect gas phase statistics. It is noted that the fraction of the resolved turbulent kinetic energy is larger than 90% in most regions of the studied flow, which indicates that reasonable results can be obtained from LES on the current mesh according to Pope's criterion [60].

The simulations in the present work are carried out using the open source CFD library OpenFOAM [61] v1912. The underlying reacting two-phase solver is based on our previous work documented in Ref. [31], which has already been validated for Al particle cloud combustion in laminar flows. This simulation cost of the Al particle jet flame is approximately 18 000 CPU hours, in which the time step is set to 1×10^{-6} s.

5. Results and discussion

The proposed Al combustion model is first validated in a single particle setup, and the predicted burning times of Al particles with different diameters are compared with the correlation from Beckstead [11]. Please see Appendix for more information. Then, in this section, detailed comparison and analysis on the Al jet flame is performed.

5.1. Comparison with experiments

5.1.1. Al_2O_3 Smoke distribution

Mie scattering technology has been proven to be an effective way to illustrate the condensed Al_2O_3 distribution in our previous study [23].

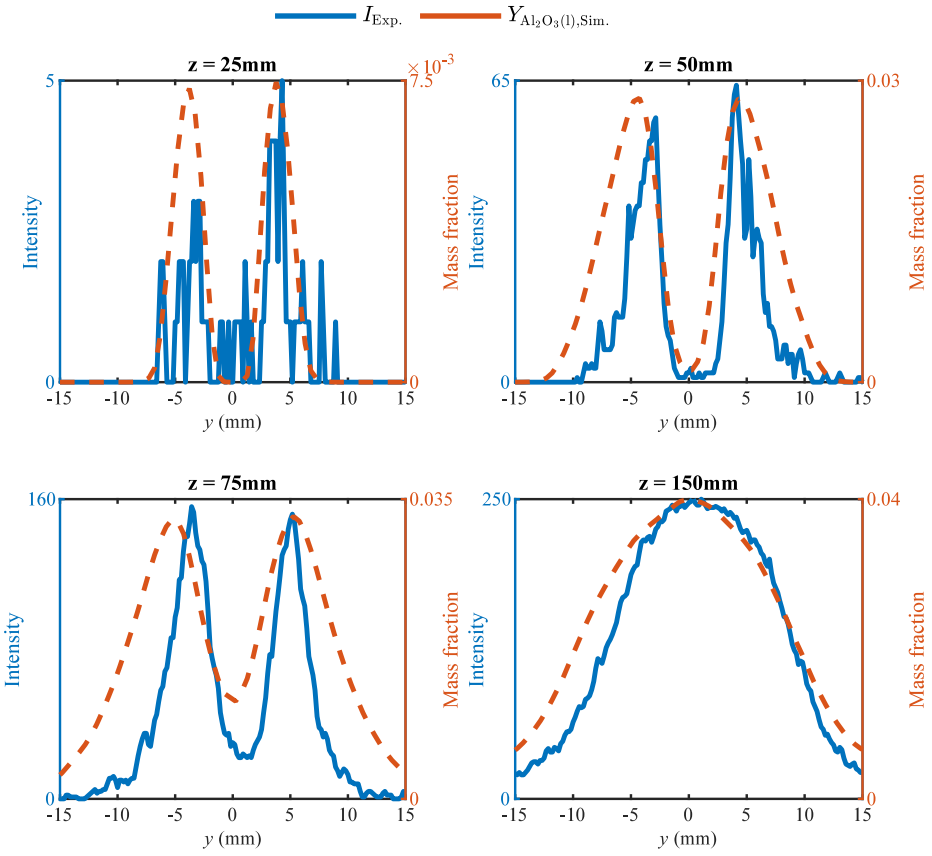

Fig. 9. Comparison of the condensed Al_2O_3 distribution measured from Mie scattering with predicted values from simulation at different heights for Case 5.

It has also been demonstrated that the Mie scattering signal in the middle and downstream region of the Al jet flame is mostly contributed by alumina smoke and the contribution from Al particles is negligible. More details can be found in our previous study [23]. Fig. 9 compares the measured Mie scattering signals from condensed Al_2O_3 ($I_{Exp.}$) and the predicted Al_2O_3(l) mass fraction ($Y_{Al_2O_3(l)}$) at different heights of the flame for Case 5. As can be seen in Fig. 9, both $I_{Exp.}$ and $Y_{Al_2O_3(l)}$ are observed to show a double-peak structure at heights of 25, 50 and 75 mm. This is because Al particles at the edge of the cloud are more fully mixed with the high-temperature post-flame gas and thus ignite and burn first, finally producing condensed Al_2O_3 in the process. Moreover, a non-zero Mie scattering signal is found in the central part of the jet at the height of 25 mm, this is because a substantial number of particles are still in the preheating stage and remain in the jet center [23], and a more detailed discussion is given in Ref. [23]. Moving downstream, the condensed $Y_{Al_2O_3}$ is observed to present a more uniform unimodal distribution at the height of 150 mm, indicating that the particles in the center of the jet are burning. Generally, the predicted condensed Al_2O_3 distribution is in good agreement with the experimental observation.

5.1.2. Temperature and H_2O concentration

Fig. 10 illustrates the comparison of the predicted gas temperature and H_2O mass fraction with the corresponding measured values from TDLAS. It is observed that there is a noticeable gap between the simulation results and the experimental measurements in the center part of the upstream and middle of the jet flame (y < 2 mm, z = 40 mm and z = 80 mm). It is indicated that the present simulation may underestimate the heat and mass transport in the center of the flame with high turbulence intensity. However, the current TDLAS optical setup tends to overestimate the temperature of the central region of the upstream of the jet flame. This is because the fluidizing gas of the Al jet is air with near-zero concentration of water vapor. Therefore the absorbance in the central region of the upstream of the jet is much smaller compared to the hot coflow. As a result, the measured temperature of the upstream of the flame is overestimated due to the influence of the surrounding hot coflow. Such bias is mainly due to the fact that the raw data measured by TDLAS is integrated along the line-of-sight. Therefore, uncertainties may be introduced to the obtained scalar profiles of the central part of the jet flame, especially when the gradient of the scalar is large. Similar findings were reported in a previous research [27] on piloted coal jet flame, in which two-color pyrometry presents much higher measured temperature along the centerline of the jet flame than simulations. To address this issue, Computed Tomography-Tunable Diode Laser Absorption Spectroscopy (CT-TDLAS) [62] can be used in the future. Moving downstream, the temperature and H_2O concentration become more uniform in space, and better agreement is achieved between simulation results and experimental measurements.

5.2. Flame structure analysis

Fig. 11(a) presents instantaneous and temporal mean temperature fields. Fig. 11(b) compares the predicted condensed Al_2O_3 mass fraction and the Mie scattering image from experiments. It is observed that the temperature of the post-flame gas remains nearly unchanged downstream of the burner outlet until the height is about 25 mm, indicating that Al particles begin to burn and release heat to the bulk gas at this height. Due to the nature of heterogeneous combustion of solid fuel particles [63] under fuel-lean conditions, the instantaneous temperature and condensed Al_2O_3 distributions present discrete characteristics. Although the peak temperature of micro flames around burning Al particles can be more than 3500 K [64,65], the temperature peak in the instantaneous snapshot is only 2700 K, which decreases to about 2200 K after time-averaging. This is because the Al jet flame under Case 5

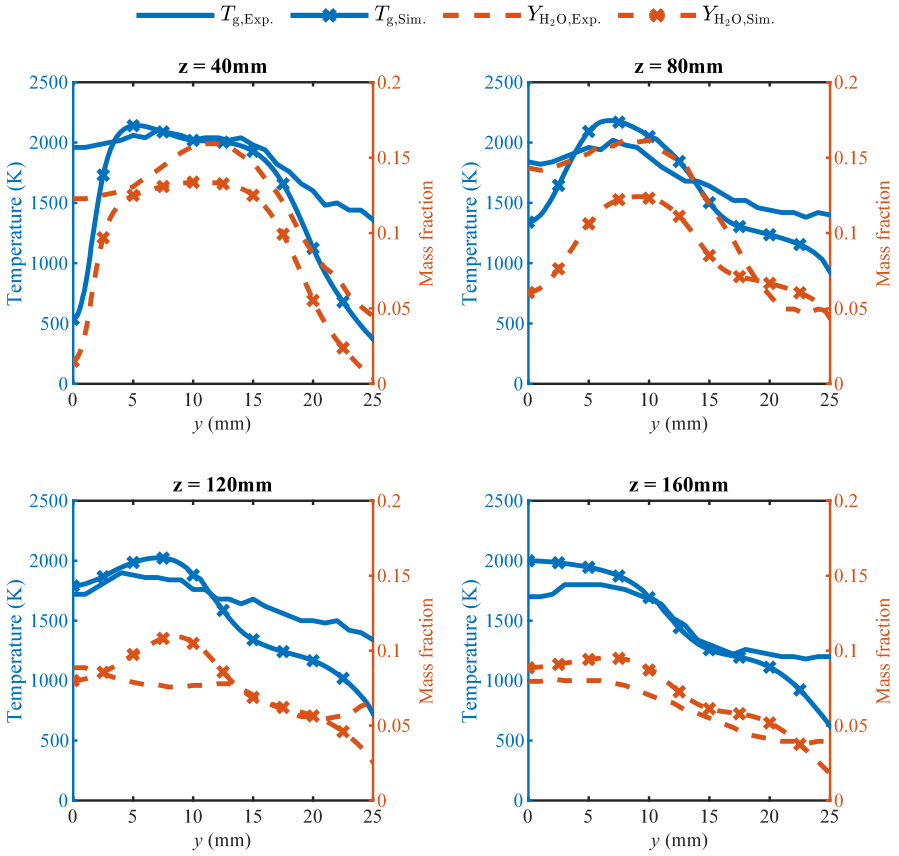

Fig. 10. Comparison of the gas temperature and H_2O concentration measured by TDLAS with corresponding predicted values at different heights for Case 5.

is very dilute, and the gas temperature calculated in present Euler–Lagrange simulation represents the average gas temperature inside one LES cell. In Case 8, the dust concentration at the particle inlet is doubled compared with Case 5, and the peak temperature of the Al jet flame can be more than 3300 K, and the average gas temperature can reach 3000 K, as shown in Fig. 12. Focusing on the condensed Al_2O_3 snapshot in Fig. 11(b), Kelvin–Helmholtz vortices are observed in the Mie scattering image due to nanoscale Al_2O_3 smoke acting as perfect flow tracer, and similar structures are found in the simulation, validating the accuracy of the present model.

Fig. 13 shows an instantaneous snapshot of the Al particle distribution, and particles are scaled by diameter and colored by temperature (left half) and liquid Al mass fraction (right half). It should be noted that particles are magnified for clarity of presentation, therefore, the particle size and spatial scale are not comparable. It can be seen that particles with a smaller diameter have a faster temperature rise and melt first (at lower height). Then, the liquid Al inside the particles is consumed by HSR in the preheating stage and further evaporation in the combustion stage, and $Y_{p,Al(l)}$ becomes zero again when particles are burnt out. Moreover, it is clearly observed that a certain number of particles with relatively large diameters still contain a substantial amount of liquid Al when they leave the computational domain, indicating incomplete combustion. Therefore, if such a laboratory-scale burner for mechanism research is to be applied to an industrial-scale power system, special attention should be paid to the design of the metal fuel combustor to improve the combustion efficiency.

5.3. Ignition distance of the Al particle jet flames

Al particles are known to have a relatively high ignition temperature [19] and thus long preheating stage, which leads to a noticeable ignition distance of the Al jet flame [23]. Therefore, in order to increase the power density of the metal fuel combustor, research on reducing the lift-off height is needed. In this sub-section, the influence of the effective oxidizer mole fraction and the initial temperature of the primary jet on the ignition distance is discussed.

In the present study, the ignition distance is defined as the height at which 10% of the injected particles are ignited ($T_p > 2327$ K). Results for 11 intermediate time steps are output during the simulation after turbulence is fully developed, and 11 ignition distances can be obtained from these time steps based on the definition mentioned above. Fig. 14 shows the average ignition distances under different effective oxidizer mole fraction conditions with error bar representing the standard deviation of the 11 samples. From Case 1 to Case 4, the effective oxidizer mole fraction is increased from 19.82% to 33.97%, as shown in Table 3, as a result, the ignition distance grows from 58.32 mm to 61.08 mm. This phenomenon is straightforward to explain, due to the rise in the oxidizer concentration, both kinetically- and diffusion-controlled HSR rates are improved, which leads to earlier ignition of Al particles.

Fig. 15 presents the ignition distances under the same co-flow condition but with different initial temperatures of the primary jet. As listed in Table 3, from Case 2, Case 6 to Case 7, the initial temperature of the primary jet, i.e. the initial temperature of the Al particles and the carrier gas, is increased from 300 K to 700 K. As a consequence, the ignition distance is decreased from 60.06 mm to 51.96 mm, which indicates that preheating the primary jet can effectively reduce the ignition distance. Therefore, using the high-temperature exhaust gas to heat the Al particles and the carrier gas is a feasible way to improve the power density of the metal fuel combustor.

6. Conclusion

In the present work, a detailed model for simulating Al particle cloud combustion with multiple oxidizers in the context of large eddy

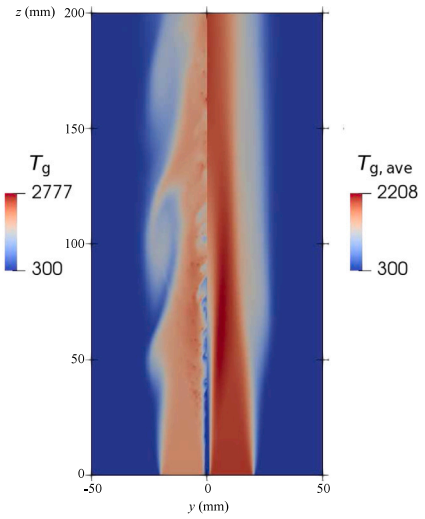

(a) Instantaneous (left half) and average (right half) image of gas temperature

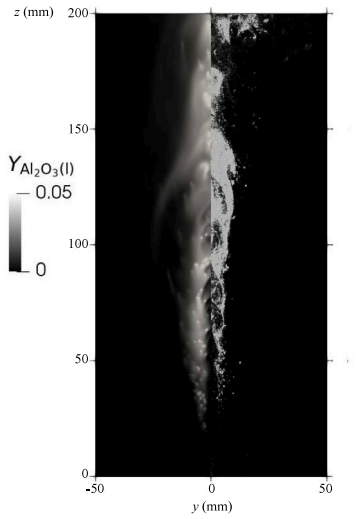

(b) Predicted condensed Al_2O_3 distribution (left) and Mie scattering image (right)

Fig. 11. Flame images for Case 5.

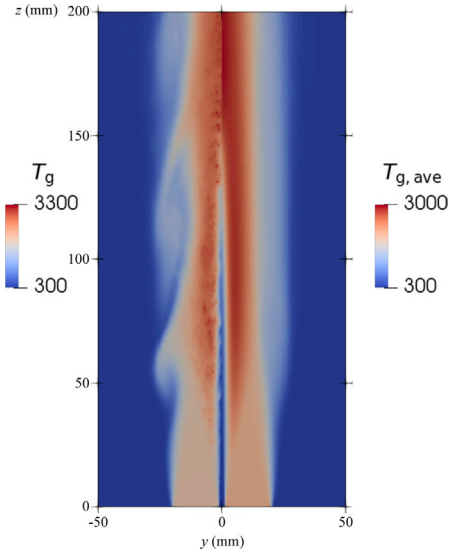

Fig. 12. Instantaneous (left half) and average (right half) image of gas temperature for Case 8.

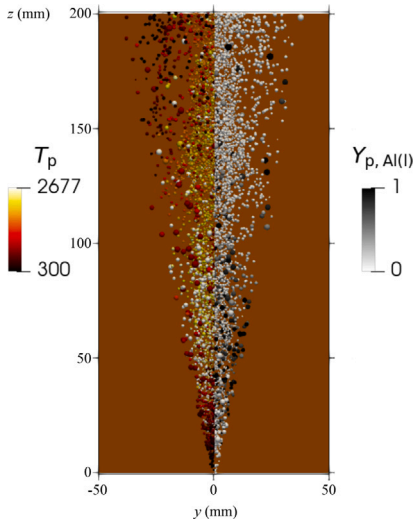

Fig. 13. Al particles scaled by diameter and colored by temperature (left half) and liquid Al mass fraction (right half) for Case 5.

simulation is developed, in which the conversion process of Al particles is divided into (1) preheating and heterogeneous reaction stage and (2) quasi-steady combustion. The Al particles are treated in a Lagrangian manner with various sub-models including phase change, heterogeneous surface reaction, evaporation and radiation. The model is implemented in OpenFOAM and then employed to simulate Al particle jet flames stabilized in a hot co-flow supported by a flat flame burner under various operating conditions. Experimental measurements including Mie scattering and Tunable diode laser absorption spectroscopy are performed for the Al particle jet flame, in which the gas phase temperature, H_2O concentration as well as the condensed Al_2O_3 distribution are obtained.

The present model is first validated by comparing the predicted condensed Al_2O_3 distribution with the measured Mie scattering signals. The results indicate that the simulation results are in good agreement

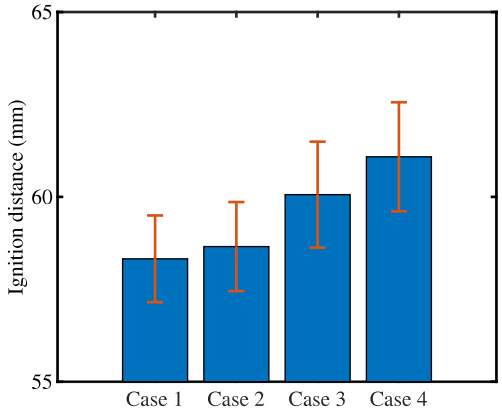

Fig. 14. Ignition distance versus effective oxidizer mole fraction.

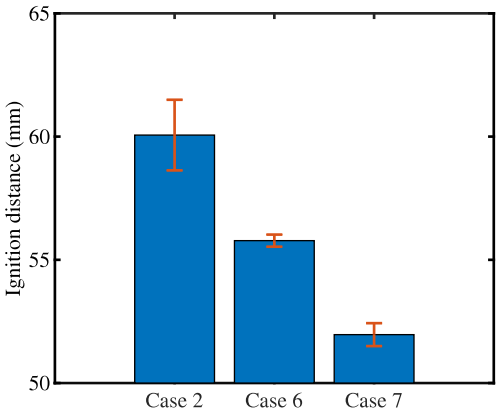

Fig. 15. Ignition distance versus initial temperature of the primary jet.

with the experimental measurements. Further comparisons of the temperature and H_2O profiles cross the flame are then conducted, and the numerical simulation results show weaker mass and heat transport in center part of the upstream and middle of the flame, in which turbulence intensity is high, compared with the reconstructed TDLAS result. It should be noted that the raw data obtained from TDLAS, which is integrated along the line-of-sight, may introduce some uncertainties to the center part of the obtained scalar profile, especially when the gradient of the scalar is large. Further detailed measurements of the flame are needed to illustrate the distribution of varying physical properties in the high turbulence region. Moreover, the predicted scalar profiles of the downstream of the jet flame agree well with the measurements.

Based on the predicted scalar profiles and the measured Mie scattering signals, the flame structure of the Al particle jet flame is analyzed. The instantaneous temperature and condensed Al_2O_3 distributions present discrete characteristics, because of the nature of heterogeneous combustion of metal fuel particles under fuel-lean conditions. Although the temperature of flame sheet around a burning Al particle can be more than 3500 K, the peak average gas temperature of the Al jet flame can peak as low as 2200 K under fuel-lean conditions. After doubling the Al particle mass feeding rate, the peak of the average gas temperature increases to about 3000 K. In addition, simulation results indicate that Al particles with large diameter cannot burn completely in the present burner. Finally, the effect of the oxidizer mole fraction and the initial temperature of the primary jet on the ignition distance is discussed according to the simulation results. It is found that increasing the oxidizer concentration of the hot co-flow or the initial temperature of the Al particles and carrier gas is an effective way to decrease the ignition distance and therefore improve the power density of the combustor.

In future research, improvements can be attempted from the following aspects. Measurements of the Al jet flame using computed tomography-tunable diode laser absorption spectroscopy is suggested, which could provided a detailed experiments database. Advanced turbulent combustion model, such as flamelet-based model, can be used to incorporate detailed chemistry kinetics into the current LES framework with acceptable computational cost.

Declaration of competing interest

The authors declare that they have no known competing financial interests or personal relationships that could have appeared to influence the work reported in this paper.

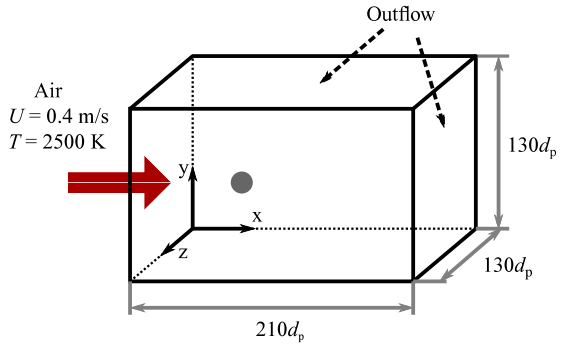

Fig. A.16. Computational domain and boundary conditions for single aluminum particle combustion.

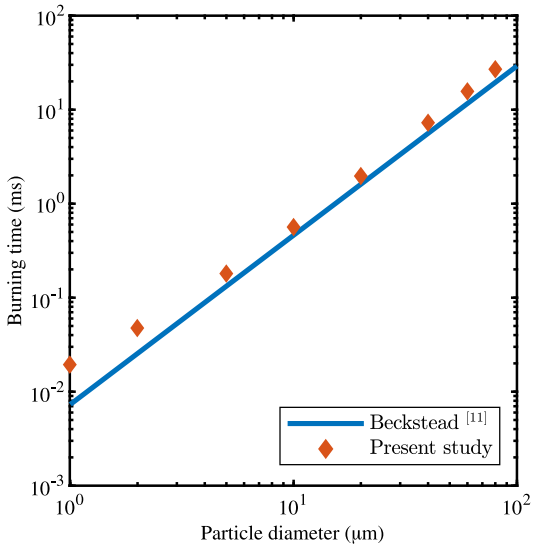

Fig. A.17. Combustion time calculated in present simulations with varying particle diameter, compared with the correlation by Beckstead [11].

Acknowledgments

The authors gratefully thank Gongxi Zhou and Renjie Li for their crucial help in the TDLAS measurement and Tien Duc Luu and Ali Shamooni for their contributions to the early stage of the implementation of the present model in OpenFOAM. This work is supported by National Natural Science Foundation of China No. 52006240, Hunan Provincial Natural Science Foundation of China Nos. 2020JJ4665 and 2021JJ30775. The support provided by China Scholarship Council (No. 201903170201) during a visit of Jiarui Zhang to University of Stuttgart is gratefully acknowledged.

Appendix. Model validation on single particle setup

A.1. Numerical configuration

A single particle setup, in which a single Al particle is heated by a hot coflow, is employed to evaluate the behavior of the various aluminum sub-models as well as their interaction in the overall combustion model. The computational domain features a cuboid and it spans $L_x = 210d_p$, $L_y = L_z = 130d_p$. As shown in Fig. A.16, a single aluminum particle is fixed in the flow field at $(55d_p, 65d_p, 65d_p)$. The domain is discretized into $21 \times 13 \times 13$ cells, which results in a mesh resolution of $10d_p$. The initial gas temperature in the domain is set to 2500 K.

Preheated air flows in from the left boundary with a fixed velocity(U) of 0.4 m/s and a temperature(T) of 2500 K. Zero-gradient outflow conditions are used for all other boundaries.

A.2. Results

In the present model, the burning time is defined as the period of time from when the particle temperature reaches the melting point of alumina until 95% of liquid aluminum inside the particle is consumed [66]. As can be seen in Fig. A.17, the predicted burning time is generally in good agreement with empirical correlations. For smaller particles, the Beckstead's correlation underestimates their burn times because their combustion is no longer purely diffusion-controlled.

References

[1] C. Muhire, A. Tesfay Reda, D. Zhang, X. Xu, C. Cui, An overview on metal oxide-based materials for iodine capture and storage, Chem. Eng. J. 431 (2022) 133816, http://dx.doi.org/10.1016/j.cej.2021.133816, URL https://www.sciencedirect.com/science/article/pii/S1385894721053900.

[2] P. Julien, J.M. Bergthorson, Enabling the metal fuel economy: green recycling of metal fuels, Sustain. Energy Fuels 1 (2017) 615–625, http://dx.doi.org/10.1039/C7SE00004A.

[3] J.M. Bergthorson, Recyclable metal fuels for clean and compact zero-carbon power, Prog. Energy Combust. Sci. 68 (2018) 169–196, http://dx.doi.org/10.1016/j.pecs.2018.05.001, URL http://www.sciencedirect.com/science/article/pii/S0360128518300327.

[4] J. Bergthorson, S. Goroshin, M. Soo, P. Julien, J. Palecka, D. Frost, D. Jarvis, Direct combustion of recyclable metal fuels for zero-carbon heat and power, Appl. Energy 160 (2015) 368–382, http://dx.doi.org/10.1016/j.apenergy.2015.09.037, URL http://www.sciencedirect.com/science/article/pii/S0306261915011071.

[5] E. Shkolnikov, A. Zhuk, M. Vlaskin, Aluminum as energy carrier: Feasibility analysis and current technologies overview, Renew. Sustain. Energy Rev. 15 (9) (2011) 4611–4623, http://dx.doi.org/10.1016/j.rser.2011.07.091, URL http://www.sciencedirect.com/science/article/pii/S1364032111003364.

[6] H. Wiinikka, T. Vikström, J. Wennebro, P. Toth, A. Sepman, Pulverized sponge iron, a zero-carbon and clean substitute for fossil coal in energy applications, Energy Fuels 32 (9) (2018) 9982–9989, http://dx.doi.org/10.1021/acs.energyfuels.8b02270, arXiv:https://doi.org/10.1021/acs.energyfuels.8b02270.

[7] T. Abu-Hamed, J. Karni, M. Epstein, The use of boron for thermochemical storage and distribution of solar energy, Sol. Energy 81 (1) (2007) 93–101, http://dx.doi.org/10.1016/j.solener.2006.06.012, URL https://www.sciencedirect.com/science/article/pii/S0038092X06001861.

[8] W. Ao, Y. Gao, S. Zhou, L.K. Li, W. He, P. Liu, Q. long Yan, Enhancing the stability and combustion of a nanofluid fuel with polydopamine-coated aluminum nanoparticles, Chem. Eng. J. 418 (2021) 129527, http://dx.doi.org/10.1016/j.cej.2021.129527, URL https://www.sciencedirect.com/science/article/pii/S1385894721011141.

[9] D.S. Sundaram, P. Puri, V. Yang, A general theory of ignition and combustion of nano- and micron-sized aluminum particles, Combust. Flame 169 (2016) 94–109, http://dx.doi.org/10.1016/j.combustflame.2016.04.005, URL http://www.sciencedirect.com/science/article/pii/S0010218016300529.

[10] E.I. Senyurt, E.L. Dreizin, At what ambient temperature can thermal runaway of a burning metal particle occur? Combust. Flame 236 (2022) 111800, http://dx.doi.org/10.1016/j.combustflame.2021.111800, URL https://www.sciencedirect.com/science/article/pii/S0010218021005435.

[11] M.W. Beckstead, Correlating aluminum burning times, Combust. Explos. Shock Waves 41 (5) (2005) 533–546, http://dx.doi.org/10.1007/s10573-005-0067-2.

[12] D.S. Sundaram, V. Yang, V.E. Zarko, Combustion of nano aluminum particles (review), Combust. Explos. Shock Waves 51 (2) (2015) 173–196, http://dx.doi.org/10.1134/S0010508215020045.

[13] J. Wang, N. Wang, X. Zou, W. Yu, B. Shi, Modeling of micro aluminum particle combustion in multiple oxidizers, Acta Astronaut. 189 (2021) 119–128, http://dx.doi.org/10.1016/j.actaastro.2021.08.047, URL https://www.sciencedirect.com/science/article/pii/S0094576521004689.

[14] S. Goroshin, I. Fomenko, J. Lee, Burning velocities in fuel-rich aluminum dust clouds, Symp. Int. Combust. 26 (2) (1996) 1961–1967, http://dx.doi.org/10.1016/S0082-0784(96)80019-1.

[15] R. Lomba, P. Laboureur, C. Dumand, C. Chauveau, F. Halter, Determination of aluminum-air burning velocities using PIV and laser sheet tomography, Proc. Combust. Inst. 37 (2019) 3143–3150, http://dx.doi.org/10.1016/j.proci.2018.07.013, URL http://www.sciencedirect.com/science/article/pii/S1540748918304310.

[16] P. Julien, J. Vickery, S. Goroshin, D.L. Frost, J.M. Bergthorson, Freely-propagating flames in aluminum dust clouds, Combust. Flame 162 (11) (2015) 4241–4253, http://dx.doi.org/10.1016/j.combustflame.2015.07.046.

[17] P. Escot Bocanegra, D. Davidenko, V. Sarou-Kanian, C. Chauveau, I. Gökalp, Experimental and numerical studies on the burning of aluminum micro and nanoparticle clouds in air, Exp. Therm Fluid Sci. 34 (2010) 299–307, http://dx.doi.org/10.1016/j.expthermflusci.2009.10.009.

[18] P. Julien, S. Whiteley, M. Soo, S. Goroshin, D.L. Frost, J.M. Bergthorson, Flame speed measurements in aluminum suspensions using a counterflow burner, Proc. Combust. Inst. 36 (2) (2017) 2291–2298, http://dx.doi.org/10.1016/j.proci.2016.06.150, URL http://www.sciencedirect.com/science/article/pii/S1540748916302085.

[19] Y. Huang, G.A. Risha, V. Yang, R.A. Yetter, Effect of particle size on combustion of aluminum particle dust in air, Combust. Flame 156 (1) (2009) 5–13, http://dx.doi.org/10.1016/j.combustflame.2008.07.018, URL http://www.sciencedirect.com/science/article/pii/S0010218008002861.

[20] D.-H. Han, H.-G. Sung, A numerical study on heterogeneous aluminum dust combustion including particle surface and gas-phase reaction, Combust. Flame 206 (2019) 112–122, http://dx.doi.org/10.1016/j.combustflame.2019.04.036, URL http://www.sciencedirect.com/science/article/pii/S0010218019301816.

[21] G. Richards, M. McMillian, R. Gemmen, W. Rogers, S. Cully, Issues for low-emission, fuel-flexible power systems, Prog. Energy Combust. Sci. 27 (2) (2001) 141–169, http://dx.doi.org/10.1016/S0360-1285(00)00019-8, URL http://www.sciencedirect.com/science/article/pii/S0360128500000198.

[22] V. Arkhipov, A. Korotkikh, A. Egorov, A. Tizilov, Features of the flame propagation rate in air stream of aluminum particles aerosuspension, in: Power Eng Effic Reliab Safety Sel Reports All-Russian Scientific and Technical Conference, 2014, pp. 98–102, http://dx.doi.org/10.13140/2.1.1433.1681.

[23] J. Zhang, Z. Xia, L. Ma, L. Huang, Y. Feng, D. Yang, Experimental study on aluminum particles combustion in a turbulent jet, Energy 214 (2021) 118889, http://dx.doi.org/10.1016/j.energy.2020.118889, URL http://www.sciencedirect.com/science/article/pii/S0360544220319964.

[24] Y. Huang, G.A. Risha, V. Yang, R.A. Yetter, Combustion of bimodal nano/micron-sized aluminum particle dust in air, Proc. Combust. Inst. 31 (2) (2007) 2001–2009, http://dx.doi.org/10.1016/j.proci.2006.08.103, URL http://www.sciencedirect.com/science/article/pii/S154074890600366X.

[25] J. Nam, J.J. Yoh, A numerical investigation of the effects of hydrogen addition on combustion instability inside a partially-premixed swirl combustor, Appl. Therm. Eng. 176 (2020) 115478, http://dx.doi.org/10.1016/j.applthermaleng.2020.115478, URL https://www.sciencedirect.com/science/article/pii/S1359431120329604.

[26] L. Ma, D. Roekaerts, Modeling of spray jet flame under MILD condition with non-adiabatic FGM and a new conditional droplet injection model, Combust. Flame 165 (2016) 402–423, http://dx.doi.org/10.1016/j.combustflame.2015.12.025.

[27] O.T. Stein, G. Olenik, A. Kronenburg, F. Cavallo Marincola, B.M. Franchetti, A.M. Kempf, M. Ghiani, M. Vascellari, C. Hasse, Towards comprehensive coal combustion modelling for LES, Flow Turbul. Combust. 90 (4) (2013) 859–884, http://dx.doi.org/10.1007/s10494-012-9423-y.

[28] F.M. Najjar, J.P. Ferry, A. Haselbacher, S. Balachandar, Simulations of solid-propellant rockets: Effects of aluminum droplet size distribution, J. Spacecr. Rockets 43 (6) (2006) 1258–1270, http://dx.doi.org/10.2514/1.17326.

[29] X. Chen, Z. Xia, L. Huang, L. Ma, Numerical simulation of a vortex combustor based on aluminum and steam, Energies 9 (12) (2016) http://dx.doi.org/10.3390/en9121072, URL http://www.mdpi.com/1996-1073/9/12/1072.

[30] K. Yamamoto, T. Murota, T. Okazaki, M. Taniguchi, Large eddy simulation of a pulverized coal jet flame ignited by a preheated gas flow, Proc. Combust. Inst. 33 (2) (2011) 1771–1778, http://dx.doi.org/10.1016/j.proci.2010.05.113, URL https://www.sciencedirect.com/science/article/pii/S1540748910002841.

[31] J. Zhang, O.T. Stein, T.D. Luu, A. Shamooni, Z. Xia, Z. Luo, L. Ma, Y. Feng, A. Kronenburg, Detailed modeling of aluminum particle combustion – from single particles to cloud combustion in bunsen flames, Chin. J. Aeronaut. (2021) http://dx.doi.org/10.1016/j.cja.2021.12.005, URL https://www.sciencedirect.com/science/article/pii/S1000936121004386.

[32] Z. Wang, X. Lin, F. Li, J. Peng, Y. Liu, Z. Zhang, S. Fang, X. Yu, Determining the time-resolved mass flow rates of hybrid rocket fuels using laser absorption spectroscopy, Acta Astronaut. 188 (2021) 110–120, http://dx.doi.org/10.1016/j.actaastro.2021.07.028, URL https://www.sciencedirect.com/science/article/pii/S0094576521003866.

[33] S. Fang, Z. Wang, X. Lin, F. Li, R. Li, J. Li, Z. Zhang, Y. Liu, X. Yu, Characterizing combustion of a hybrid rocket using laser absorption spectroscopy, Exp. Therm Fluid Sci. 127 (2021) 110411, http://dx.doi.org/10.1016/j.expthermflusci.2021.110411, URL https://www.sciencedirect.com/science/article/pii/S0894177721000625.

[34] H. Shen, Y. Wu, K. Xu, P.J. Smith, H. Zhang, Eulerian LES simulation of coal jet flame with a simplified DQMOM model, Fuel 216 (2018) 475–483, http://dx.doi.org/10.1016/j.fuel.2017.12.003, URL http://www.sciencedirect.com/science/article/pii/S0016236117315703.

[35] J. Smagorinsky, General circulation experiments with the primitive equations: I. The basic experiment, Mon. Weather Rev. 91 (3) (1963) 99–164, http://dx.doi.org/10.1175/1520-0493(1963)091<0099:GCEWTP>2.3.CO;2, URL https://journals.ametsoc.org/view/journals/mwre/91/3/1520-0493_1963_091_0099_gcewtp_2_3_co_2.xml.

[36] H. Pitsch, H. Steiner, Scalar mixing and dissipation rate in large-eddy simulations of non-premixed turbulent combustion, Proc. Combust. Inst. 28 (1) (2000) 41–49, http://dx.doi.org/10.1016/S0082-0784(00)80193-9, URL https://www.sciencedirect.com/science/article/pii/S0082078400801939.
[37] M.C. Yuen, L.W. Chen, On drag of evaporating liquid droplets, Combust. Sci. Technol. 14 (4–6) (1976) 147–154, http://dx.doi.org/10.1080/00102207608547524.
[38] M. Bini, W. Jones, Large-eddy simulation of particle-laden turbulent flows, J. Fluid Mech. 614 (2008) 207–252, http://dx.doi.org/10.1017/S0022112008003443.
[39] W.P. Jones, A.J. Marquis, D. Noh, An investigation of a turbulent spray flame using large eddy simulation with a stochastic breakup model, Combust. Flame 186 (2017) 277–298, http://dx.doi.org/10.1016/j.combustflame.2017.08.019, URL http://www.sciencedirect.com/science/article/pii/S0010218017303164.
[40] W.E. Ranz, W.R. Marshall, Evaporation from drops, Chem. Eng. Prog. 48 (3) (1952) 141–146.
[41] C.T. Crowe, J.D. Schwarzkopf, M. Sommerfeld, Y. Tsuji, Multiphase Flows with Droplets and Particles, second ed., CRC Press, Boca Raton, 2011.
[42] M. Chase, NIST-JANAF Thermochemical Tables, American Institute of Physics, Melville, 1998, URL https://janaf.nist.gov/.
[43] X. Mi, A. Fujinawa, J.M. Bergthorson, A quantitative analysis of the ignition characteristics of fine iron particles, Combust. Flame 240 (2022) 112011, http://dx.doi.org/10.1016/j.combustflame.2022.112011, URL https://www.sciencedirect.com/science/article/pii/S001021802200030X.
[44] M.F. Modest, Radiative Heat Transfer, third ed., Academic Press, Pittsburgh, 2013.
[45] J. Guo, L. Shen, X. He, Z. Liu, H. Im, Assessment of weighted-sum-of-gray-gases models for gas-soot mixture in jet diffusion flames, Int. J. Heat Mass Transfer 181 (2021) 121907, http://dx.doi.org/10.1016/j.ijheatmasstransfer.2021.121907.
[46] T. Kangwanpongpan, F.H.R. França, R. Corrêa da Silva, P.S. Schneider, H.J. Krautz, New correlations for the weighted-sum-of-gray-gases model in oxy-fuel conditions based on HITEMP 2010 database, Int. J. Heat Mass Transfer 55 (25) (2012) 7419–7433, http://dx.doi.org/10.1016/j.ijheatmasstransfer.2012.07.032, URL http://www.sciencedirect.com/science/article/pii/S0017931012005686.
[47] P. Lynch, H. Krier, N. Glumac, Emissivity of aluminum-oxide particle clouds: application to pyrometry of explosive fireballs, J. Thermophys. Heat Transfer 24 (2) (2010) 301–308, http://dx.doi.org/10.2514/1.43853.
[48] J. Harrison, M.Q. Brewster, Simple model of thermal emission from burning aluminum in solid propellants, J. Thermophys. Heat Transfer 23 (3) (2009) 630–634, http://dx.doi.org/10.2514/1.39143, arXiv:https://doi.org/10.2514/1.39143.
[49] M. Rieth, F. Proch, M. Rabacal, B. Franchetti, F.C. Marincola, A. Kempf, Flamelet LES of a semi-industrial pulverized coal furnace, Combust. Flame 173 (2016) 39–56, http://dx.doi.org/10.1016/j.combustflame.2016.07.013.
[50] P.E. DesJardin, J.D. Felske, M.D. Carrara, Mechanistic model for aluminum particle ignition and combustion in air, J. Propul. Power 21 (3) (2005) 478–485, http://dx.doi.org/10.2514/1.5864.
[51] J.C. Hewson, V.F. Nicolette, Predicting Aluminum Droplet Burning Rates with Varying Oxidizers, United States, 2008, arXiv:SponsorOrg.:USDOENationalNuclearSecurityAdministration(NNSA). URL https://www.osti.gov/servlets/purl/1145687.
[52] I. Glassman, R.A. Yetter, N.G. Glumac, in: I. Glassman, R.A. Yetter, N.G. Glumac (Eds.), Combustion, fifth ed., Academic Press, Boston, 2015.
[53] M.K. King, Modeling of single particle aluminum combustion in CO2-N2 atmospheres, Symp. Int. Combust. 17 (1) (1979) 1317–1328, http://dx.doi.org/10.1016/S0082-0784(79)80124-1, URL https://www.sciencedirect.com/science/article/pii/S0082078479801241. Seventeenth Symposium (International) on Combustion.
[54] J. Glorian, S. Gallier, L. Catoire, On the role of heterogeneous reactions in aluminum combustion, Combust. Flame 168 (2016) 378–392, http://dx.doi.org/10.1016/j.combustflame.2016.01.022, URL http://www.sciencedirect.com/science/article/pii/S0010218016000377.
[55] L. Zhou, L. Hu, F. Wang, Large-eddy simulation of turbulent combustion using different combustion models, Fuel 87 (13) (2008) 3123–3131, http://dx.doi.org/10.1016/j.fuel.2008.04.025, URL https://www.sciencedirect.com/science/article/pii/S0016236108001774.
[56] A. Fontijn, W. Felder, HTFFR kinetics studies of Al+CO2→AlO+CO from 300 to 1900 K, a non-arrhenius reaction, J. Chem. Phys. 67 (4) (1977) 1561–1569, http://dx.doi.org/10.1063/1.434986, arXiv:https://doi.org/10.1063/1.434986.
[57] S. Akaotsu, Y. Matsushita, H. Aoki, W. Malalasekera, Application of flamelet/progress-variable approach to the large eddy simulation of a turbulent jet flame of pulverized coals, Adv. Powder Technol. 31 (10) (2020) 4253–4274, http://dx.doi.org/10.1016/j.apt.2020.09.005, URL https://www.sciencedirect.com/science/article/pii/S0921883120304246.
[58] L. Ma, D. Roekaerts, Structure of spray in hot-diluted coflow flames under different coflow conditions: A numerical study, Combust. Flame 172 (2016) 20–37, http://dx.doi.org/10.1016/j.combustflame.2016.06.017.
[59] Y. Feng, Z. Xia, L. Huang, L. Ma, Ignition and combustion of a single aluminum particle in hot gas flow, Combust. Flame 196 (2018) 35–44, http://dx.doi.org/10.1016/j.combustflame.2018.05.010, URL https://www.sciencedirect.com/science/article/pii/S0010218018302049.
[60] S.B. Pope, Ten questions concerning the large-eddy simulation of turbulent flows, New J. Phys. 6 (2004) 35, http://dx.doi.org/10.1088/1367-2630/6/1/035.
[61] H.G. Weller, G. Tabor, H. Jasak, C. Fureby, A tensorial approach to computational continuum mechanics using object-oriented techniques, Comput. Phys. 12 (6) (1998) 620–631, http://dx.doi.org/10.1063/1.168744, arXiv:https://aip.scitation.org/doi/pdf/10.1063/1.168744.
[62] Z. Wang, T. Kamimoto, Y. Deguchi, W. Zhou, J. Yan, K. Tainaka, K. Tanno, H. Watanabe, R. Kurose, Two dimensional temperature measurement characteristics in pulverized coal combustion field by computed tomography-tunable diode laser absorption spectroscopy, Appl. Therm. Eng. 171 (2020) 115066, http://dx.doi.org/10.1016/j.applthermaleng.2020.115066, URL https://www.sciencedirect.com/science/article/pii/S1359431119330571.
[63] F. Lam, X. Mi, A.J. Higgins, Front roughening of flames in discrete media, Phys. Rev. E 96 (2017) 013107, http://dx.doi.org/10.1103/PhysRevE.96.013107.
[64] Z. Hu, T. Yang, Z. Xia, L. Ma, M. Li, Y. Feng, The simulation of different combustion stages of micron-sized aluminum particles, Appl. Sci. 11 (4) (2021) http://dx.doi.org/10.3390/app11041774, URL https://www.mdpi.com/2076-3417/11/4/1774.
[65] P. Bucher, R. Yetter, F. Dryer, T. Parr, D. Hanson-Parr, E. Viceni, Flames structure measurement of single, isolated aluminum particles burning in air, Symp. Int. Combust. 26 (2) (1996) 1899–1908, http://dx.doi.org/10.1016/S0082-0784(96)80012-9, URL http://www.sciencedirect.com/science/article/pii/S0082078496800129.
[66] V. Emelyanov, I. Teterina, K. Volkov, Dynamics and combustion of single aluminium agglomerate in solid propellant environment, Acta Astronaut. 176 (2020) 682–694, http://dx.doi.org/10.1016/j.actaastro.2020.03.046, URL https://www.sciencedirect.com/science/article/abs/pii/S0094576520301740.